Surface & Coatings Technology 495 (2025) 131555

Contents lists available at ScienceDirect

Surface & Coatings Technology

journal homepage: www.elsevier.com/locate/sct

Full length article

Graphene-reinforced titanium coatings deposited by Cold Gas Spray: Study of microstructure, mechanical and wear properties

Edwin Torres Díaz [a,b], Alessio Silvello [a,*], Edwin Rua Ramirez [a,b], Rafael Molero Campos [c], Antonio Paton Carrero [c], Rodolpho Fernando Vaz [a,d], Irene García Cano [a]

[a] Thermal Spray Centre (CPT), Universitat de Barcelona, C/ Martí i Franquès, 1, Barcelona, Spain
[b] Engineering Research and Development Group in New Technologies (GIDINT), Santo Tomás University, Tunja, Colombia
[c] Graphenano Nanotechnologies S.L., C/ Ctra. de Villena, km 0, 75, Yecla (Murcia), Spain
[d] Center for Thermal Spray Research (CTSR), Stony Brook University, Room 130 Heavy Engineering Bldg., Stony Brook, NY, United States

ARTICLE INFO

Keywords:
Graphene
Metal matrix
Composites
Cold spray
Corrosion
Heat treatments
Conductivity
Herringbone carbon nanoFibers
Carbon nanotubes
Reinforcement material
Coatings
Ball milling

ABSTRACT

This study integrates graphene-based nanostructures as reinforcement in a Ti matrix to produce coatings using the Cold Gas Spray (CGS) technique, aiming to enhance mechanical and tribological properties while overcoming some of the limitations of conventional thermal spray methods. The hypothesis holds that incorporating Carbon Nanofibers (GFs) into Ti matrices significantly reinforces these properties compared to pure Ti coatings. The study employed ball milling for the powders obtaining, CGS deposition, and various analytical tests to evaluate the performance of Ti-GFs and pure Ti coatings. Results revealed that Ti-GFs coatings significantly improved in mechanical properties, achieving ultimate tensile strength up to 456 MPa and a strain increase to 2.27%. These improvements are attributed to effective load transfer across the Ti-GFs interfaces, facilitated by strong chemisorption interactions. Additionally, heat treatments at 1000 °C relieved residual stresses and promoted microstructural changes via atomic diffusion, further contributing to the coatings' strength and ductility. Tribological assessments revealed a 21% reduction in the coefficient of friction for Ti-GFs coatings compared to as-sprayed Ti, though was 2% higher than that of Ti-Bulk. This suggests the potential of graphene as a nanoscale lubricant, though further optimization of GFs dispersion and interface interactions may result in even lower coefficient.

These findings highlight the potential of GFs reinforced metal matrix composites applied by CGS for critical applications in sectors such as aerospace and biomedical, which demand materials with high strength and reduced mechanical wear. The study also identifies key areas for future research, including the optimization of graphene dispersion and interface bonding, to fully exploit the benefits of GFs in CGS coatings.

1. Introduction

In materials science, Graphene (GR) is considered a two-dimensional allotrope, consisting of a single layer of carbon atoms arranged in a hexagonal lattice. This configuration endows GR with unique and atypical properties [1]. Multiple methods have been developed to synthesize GR, resulting in different molecular structures: nanoscale platelets, single and multi-layered, and molecular structures in the form of fibers. Martin Gullon et al. describe various filament-like structures, composed of tiny layers of GR assembled, which form multiple bidirectional structures of GFs, each with specific potential applications [2,3]. These characteristics have facilitated the incorporation of GR into Metal Matrix Composites (MMCs), driving research in the field of engineering and offering improvements in structural, mechanical, and tribological properties, among others. This integration has significantly expanded the scope and possibilities of applications in aerospace, automotive, electronics, and biomedical sectors [4–6].

Among the techniques to deposit coatings, CGS technology [7] emerges as a revolutionary method in materials engineering, enabling the efficient deposition of coatings and the generation of GR-reinforced MMCs. CGS involves accelerating particles to supersonic speeds using a high-pressure carrier gas at a moderate temperature, allowing the particles to impact and adhere to the substrate. This process almost does not alter the feed material's properties since the powder remains all the time below its recrystallization temperature [8,9], meaning the mechanism leading to the adhesion between the particles and the substrate is based on the severe and extremely fast plastic deformation of the material and not on melting. It results in an advantage for CGS: deposition of oxygen-sensitive materials, such as Ti alloys.

* Corresponding author.
E-mail address: asilvello@cptub.eu (A. Silvello).

https://doi.org/10.1016/j.surfcoat.2024.131555
Received 15 May 2024; Received in revised form 6 September 2024; Accepted 11 November 2024
Available online 19 November 2024

Glossary

σ_u	Ultimate Tensile Strength
σ_y	Yield Stress
ϵ	Deformation
E	Elastic Modulus
CGS	Cold Gas Spray
CoF	Friction Coefficient
EDS	Energy Dispersive X-ray Spectroscopy
GFs	Carbon Nanofibers
GNPs	Nano-platelets Graphene
GR	Graphene
HCNFs	Herringbone Carbon Nanofibers
HT	Heat Treatments
LS	Laser Scattering
MMCs	Metal Matrix Composites
MWCNTs	Multi-walled Carbon Nanotube
OM	Optical Microscope
Ra	Arithmetic Average Roughness
SEM	Scanning Electron Microscopy
TEM	Transmission Electron Microscopy
XRD	X-ray Diffractometry

The importance of this research lies on the possibility of obtaining unique coating properties that are not achievable through conventional thermal spraying.

Given the limited availability of specific research on Ti coatings reinforced with one-dimensional (1D) crystalline materials from GFs and then deposited via CGS, this study builds on previous investigations focused on the incorporation of materials with two-dimensional (2D) crystalline structures, such as nano-platelets Nano-platelets Graphene (GNPs) and GFs respectively [10], used as reinforcement material in different MMCs using other techniques.

Among the key contributions in CGS GR-reinforced MMCs coatings, Prasad et al. highlights the development of metal-GR for wear, corrosion resistant and antibacterial applications [11–13]. They discuss two main techniques for preparing feedstock materials for CGS: ball milling [14] and in situ reduction [15]. They also highlight three main gaps: (i) The difficulty in achieving uniform dispersion of nanoplanar GNPs in metal powders; (ii) The need to optimize composite powders to preserve the structure of GNPs, crucial for material efficacy; and (iii) The importance of understanding the interfacial bonding between GNPs and the metal matrix, fundamental to improving the properties of the compound and the manufacturing process. These challenges highlight key areas for future research in this field [16].

In the field of GR-reinforced MMCs, a notable study conducted by Zhang et al. addresses the uniform dispersion of GNPs in a pure Ti matrix to enhance the strength and ductility of the composites. This work stands out for overcoming the limitations of pure Ti low mechanical strength in biomedical and engineering applications. Using a 3D vibration ball milling technique, a homogeneous dispersion of the GNPs, exfoliated in situ using high-purity graphite balls, was achieved. The resulting composites exhibited significant improvements in tensile strength, yield strength, elongation, and microhardness, with increases of 42.8, 20.2, 12.6, and 9.6%, respectively, compared to pure Ti. These improvements are attributed to the load transfer from the uniformly dispersed GNPs and the effect of in situ generated TiC fixation. Moreover, the study demonstrates that high-purity graphite balls are a suitable carbon source for 3D vibration milling, resulting in a uniform and efficient dispersion of GNPs [17].

Despite these advancements in the field of GR-reinforced MMCs, there is a noticeable lack of specific studies on CGS GFs reinforced Ti coatings. This gap is underscored by the limited exploration of the interactions and specific properties of GFs in Ti coatings under the unique conditions offered by CGS, which promises to preserve the intrinsic properties of GR more effectively during the processing, such as its mechanical strength, high conductivity, and critical aspects for advanced applications in sectors like aerospace and biomedical [18]. To address this gap, the present study aims to investigate the properties and behavior of CGS GFs reinforced Ti coatings with one-dimensional (1D) materials derived from GR, such as GFs.

The central hypothesis of this study is that the addition of 1D GR in Ti coatings via CGS results in significant improvements in mechanical and tribological properties, compared to conventional thermal spray methods. To test this hypothesis, the study not only focuses on evaluating the mechanical properties of the coatings, but will also include a detailed analysis of the residual stress state and crystalline microstructure, observing changes in the crystallite size. These additional analyses provide deeper insights into the structural integrity and performance of the coatings, offering a more comprehensive understanding of their behavior under various conditions.

2. Materials and methods

2.1. Materials

2.1.1. Ti powder

The matrix feedstock powder was Ti grade 1 (CNPC, Shanghai, China) manufactured in accordance with ASTM B348-13 [19]. It was characterized regarding the particle size distribution by Laser Scattering (LS) in dry mode on an LS13320 (Beckman Coulter, Brea, CA, USA) equipment, in accordance with ASTM B822-02 [20]; flowability using a Hall Flowmeter Funnel with a 2.5 mm orifice and 50 g samples, in accordance with ASTM B213-20 [21]; and particle shape using Scanning Electron Microscopy (SEM) on a Phenom ProX G6 (Thermo Scientific Eindhoven, the Netherlands) equipment with an integrated Energy Dispersive X-ray Spectroscopy (EDS) detector and X-ray Diffractometry (XRD) on an X'Pert PRO MPD (PANalytical, Malvern, United Kingdom) instrument with Co kα emissor, α = 1.7903 Å, work power of 45 kV and 40 mA, from 5 to 120° 2θ with a 0.017° step, and 80 s per step. Rietveld refinement was done to the X-ray diffraction patterns using the Materials Analysis Using Diffraction (MAUD) software. LaB6 was used as a standard to determine the instrumental error.

2.1.2. Carbon nanofibers (GFs)

Two types of GFs were selected: Herringbone Carbon Nanofibers (HCNFs), and Multi-walled Carbon Nanotube (MWCNTs); supplied by GraphenanoS.L. (Yecla, Murcia, Spain). The GFs were characterized by Raman spectroscopy using a LabRam HR 800 (Jobin-Yvon, Longjumeau, France) coupled with an BXFM Optical Microscope (OM) (Olympus, Tokyo, Japan); Transmission Electron Microscopy (TEM) using a 1010 (Jeol, Tokyo, Japan) equipped with an Orius CCD camera (Gatan, Walnut Creek, CA, USA), and high resolution scanning electron microscopy SEM on a JSM-7001F (Jeol, Tokyo, Japan) with secondary electron (SE) and backscattered electron (BSE) detectors.

2.1.3. Substrates

Ti grade 2 sheets, Ti-Bulk, measuring 20 × 50 × 5 mm^3, previously gritblasted with alumina, were used as substrates for CGS depositions. The roughness of these substrates was measured to be Arithmetic Average Roughness (Ra) > 7.0 ± 0.3 μm.

2.2. Procedures and techniques

2.2.1. Preparation of Ti-GFs reinforced powders

Two different preparations of Ti-GFs powder were conducted, referenced as follows: Ti-HCNFs and Ti-MWCNTs, with a concentration of

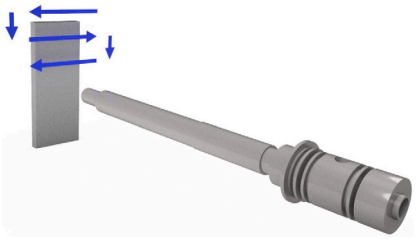

Fig. 1. CGS deposition strategy.

Table 1
Grinding and spraying parameters.

Grinding parameters		Spraying parameters	
Powder	Ti GFs	Substrate	Ti G2
Size (μm)	32.71	Robot traverse speed (mm/s)	500
Quantity (g)	200	Step (mm)	1.0
Angular speed (rpm)	200	Spraying distance (mm)	30
Ball diameter (mm)	1.0	Pressure (MPa)	6.0
Ball material	ZnO2	Temperature (°C)	1000
Weight ratio	1:2	Dosing angular speed (rpm)	2.0
Container (ml)	2 × 125		
Time (min)	90		

0.5wt% GFs. The procedure for preparing these composite powders was structured in four stages (dispersion, mixing, drying, and planetary ball milling), designed to ensure the homogenization and dispersion of the GFs within the Ti matrix.

Dispersion: In two glass containers, 1000 ml of ethanol with 1 g of HCNFs and 1 g of MWCNTs, respectively, were added, and dispersion was performed by ultrasound for a time of 60 min with 3000865 (JP Selecta, Albera, Barcelona, Spain) equipment with a power of 360 W and frequency of 40 kHz.

Mixing: 200 g of Ti was added to each container. This mixture was taken to a mechanical stirrer F20100152 (Velp, Usmate, Italy) with a dispersion disk (paddle type) at an angular speed of 500 rpm for 30 min.

Drying: The solution was decanted in a filtration funnel with a 10 μm filter paper, and after 4 h, the ethanol had completely drained from the mixture, leaving a wet mass which was taken to a UFE400 (MEMMERT, Büchenbach, Germany) oven at a temperature of 60 °C for a time of 4 h, until the ethanol content completely evaporated.

Milling: The grinding of the prepared powders was carried out using a PM 400 planetary mill (RETSCH, Haan, Germany) and balls of 1 mm in diameter; the grinding parameters are described in Table 1.

2.2.2. The CGS process

The deposition process was carried out using a PCS100 (Plasma Giken, Saitama, Japan) equipment, operating under the conditions detailed in Table 1. IRB1500 (ABB, Zurich, Switzerland) robotic arm with six degrees of freedom was employed to move the substrate, with static CGS gun. Three coatings were obtained with the supply of the prepared powders: pure Ti, Ti-HCNFs, and Ti-MWCNTs (see Fig. 1).

2.2.3. Heat treatments

Heat Treatments (HT) were conducted through annealing in a GHA 12/450 (Carbolite, Hope, England) horizontal tubular furnace, under a controlled vacuum atmosphere and an Ar environment. This setup was devised to minimize the oxidation of the samples during HT. The selected temperature range for the HT was from 500 to 1200 °C. This broad temperature range was set to thoroughly investigate the microstructural transformations and their effects on the conductive, mechanical, and physical properties of the material. The coatings underwent a temperature increase at a ramp-up rate of 10 °C/min until the annealing temperature was reached. At each stage, the temperature was held constant for 3 h and then the samples were slowly cooled for over 12 h to reach room temperature. This gradual cooling process was crucial to prevent thermal shocks and ensure a homogeneous transition of the microstructural properties.

2.2.4. Characterization of the coatings

The metallographic preparation of the coatings was conducted according to the ASTM E1920-03 standard [22]. The cross-sectional microstructure was observed using a DMI5000 M microscope (Leica, Wetzlar, Germany) equipped with a DFC290 HD digital optical camera. Porosity was determined by applying grayscale thresholding to the images, with an average of the porosity from ten images at 200x magnification, in accordance with Test Method B of ASTM E2109-14 [23]. Kroll's solution was utilized for the chemical etching of the coatings, with an immersion time of 5 s. Vickers microhardness was measured on the coatings' cross-section, using an HMV (Shimadzu, Tokyo, Japan) equipment with a load of 200 g for 15 s, in accordance with ASTM E384-99 standard [24].

2.2.5. Tensile test

The preparation of specimens for the tensile test was conducted according to the specifications set by ASTM E8/E8M standards [25], aimed at configuring flat specimens. The tensile test utilized the Instron universal testing machine, 3366 (Instron, Norwood, MA, USA), equipped with an Interface brand load cell 1210CFF (Scottsdale, AZ, USA), with a capacity of 10 kN and a force measurement accuracy of ±0.5% of the measured value up to 1/200 of the cell's capacity. A static axial extensometer, model 2630, with a sensitivity of 2.5 ± 20% (mV/V) and a travel range of −5 to +5 mm, was incorporated for deformation measurement. The software interface used for static tests was Bluehill Universal, meeting ASTM E83, ISO 9513 standards [20,26]. The test speed was set at 0.2 mm/min.

2.2.6. Wear test (ball-on-disk)

To assess the sliding wear properties of the obtained coatings, the "ball-on-disk" wear technique was implemented on equipment manufactured by CM4 Enginierya SL (Cervello, Spain), following the ASTM G99-04 standard [27]. The surfaces of the samples were prepared to achieve a maximum surface roughness Ra of 0.8 μm. The test was carried out at a constant temperature of 23 ± 2 °C and relative humidity of 50 ± 5%. A total of 22,000 wear cycles were performed, covering a total distance of one kilometer with a trajectory diameter of 14 mm. During the test, a normal load of 10 N was applied to a WC-Co ball, which slid over the coating under unlubricated conditions. The Friction Coefficient (CoF) between the ball and the coating was continuously measured and the wear rate was measured following the ASTM G99-04 standard [27] procedure.

3. Results and discussion

3.1. Characterization of the powders

The detailed characterization of the Ti powder was conducted, revealing significant features. Fig. 2a shows the powder's irregular morphology, typical of the water atomization process, where the dynamic interactions between the molten metal and the aqueous medium cause an abrupt and uneven solidification, resulting in a notably irregular shape [28].

Fig. 8 displays the Ti powder diffraction patterns, featuring eight significant peaks of the Ti α phase. The most prominent peak, observed at 40.171° with an absolute intensity of 166 638, corresponds to the (101) plane, indicating the sample's predominant phase, associated with a compact hexagonal crystalline structure (HCP) consistent with

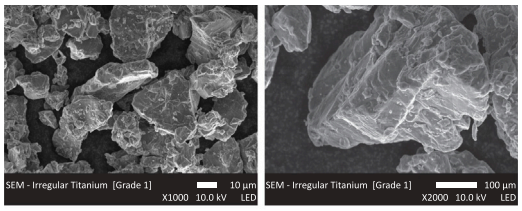

(a) SEM images of particle shape.

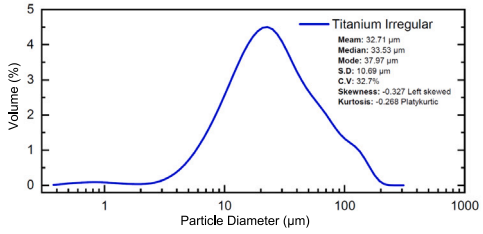

(b) Particle Size distribution.

Fig. 2. Characterization of the feedstock powder.

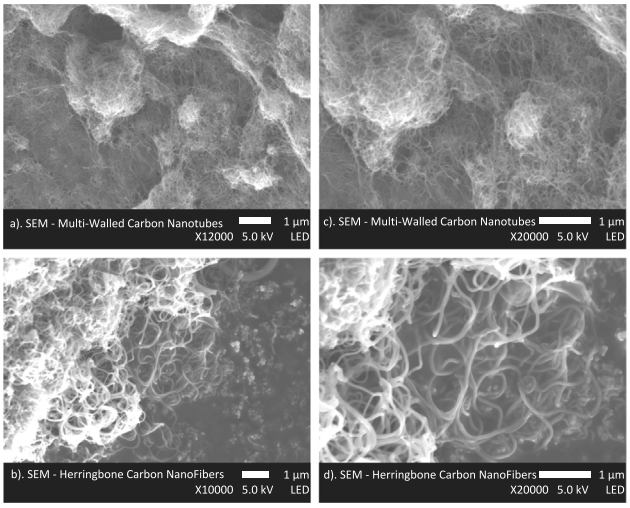

Fig. 3. SEM images of GFs. (a) HCNFs. (b) MWCNT. (c,d) high magnification.

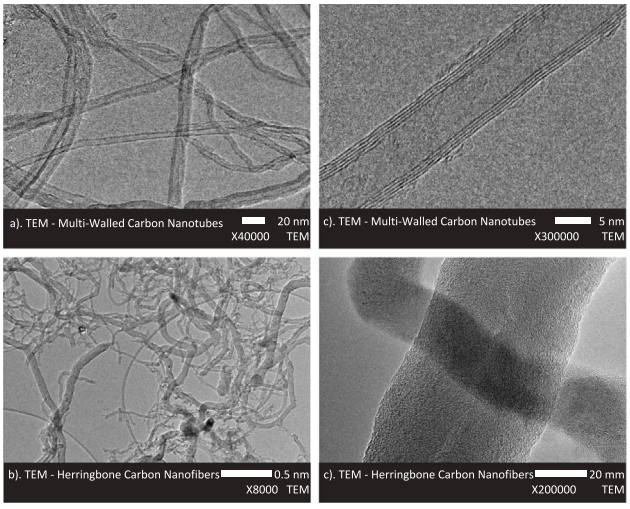

Fig. 4. TEM images of GFs. (a) HCNFs. (b) MWCNT. (c,d) high magnification.

the Ti α phase. Fig. 2b shows the Ti powder particle size distribution with a mean size of 32.71 µm, d_{10} of 8.56 µm, and d_{90} of 81.44 µm; however, even with a high d_{90} value in volume, 78% of the particles were smaller than 50 µm, showing this Ti powder adequate for the CGS deposition, as shown by Schmidt et al. who presented −60+10 µm as the best range of particle size for CGS due to their ability to reach the critical velocity for the particle bonding mechanism [29].

3.2. Characterization of carbon nanofibers

Fig. 3 presents SEM images of HCNFs and MWCNTs. Both GFs types exhibit a tendency to cluster; however, a marked difference in their morphologies is noted, with HCNFs showing denser entanglement, likely from variations in their synthesis methods. Contrastingly, MWCNTs show a more aligned and less tangled morphology; additionally, TEM images seen in Fig. 4 offer deeper insights into the structures and organization of the atomic planes of both fiber types. MWCNTs reveal their distinctive and aligned morphology, a hallmark of nanotubes, showcasing their cylindrical and laminar multi-layer winding structure with axial alignment of atomic planes; fiber diameters average between 7.0 to 12.0 nm. Furthermore, reduced densification is noted, owing to the nanotube's central void. Alternatively, HCNFs display more variable diameters ranging from 15 to 70 nm, with a noticeable presence of more robust fibers. Moreover, the sequential organization of the herringbone structure is clearly visible. Despite a small void at the center, their densification is significantly higher compared to MWCNTs. Furthermore, using Raman spectroscopy, Fig. 7, shows characteristic peaks, like the G peak associated with in-plane carbon atom vibrations, the D peak linked to structural defects and disorder, and the 2D peak providing layer count information, are observed. Raman spectroscopy has, therefore, been crucial for verifying the existence of GFs, especially after the CGS deposition, which can induce structural changes and alterations in material properties. It has been fundamental to correlate these data with the results from SEM and TEM to obtain a complete understanding of the structure and quality of the present GFs.

3.3. Characterization of Ti-GFs

SEM images shown in Fig. 5 present a visual comparison of the Ti powder reinforced with the two types of GFs, revealing the interaction Ti-GFs. Nano fibers are evident on most surfaces of the Ti particles, although the distribution is heterogeneous, leading to greater accumulations on geometrically irregular shapes prone to it. Additionally, agglomerated and entangled fibers are observed to impede a complete dispersion flattening on the particle surfaces due to impacts and friction in the milling process.

The XRD patterns represented in Fig. 8 indicate that, despite the incorporation of the GFs, the crystalline structure of Ti remains unchanged, with the characteristic peaks of the Ti α phase clearly identifiable, without significant deviations, no variations in peak width, or the generation of new peaks. Despite the milling process's intensity, it suggests that it introduces no contaminants, secondary phases, or alterations to the Ti's crystalline microstructure. Raman spectroscopy evaluation Ti-HCNFs powders, Ti-HCNFs and Ti-MWCNTs, confirms the preservation of the characteristic GR spectrum on the powder surface after milling. The Raman spectra shown in Fig. 7 display the G and 2D bands characteristic of GR, alongside the D band associated with defects or disorders in the carbon structure.

3.4. Characterization of the coatings

Coatings produced by CGS exhibited good adherence to the substrate, without peeling or cracking at the coating/substrate interface during the depositions or their subsequent cooling. Fig. 6 exemplifies the final outcome of the depositions, presenting a coating made by cold spraying of Ti, given that the Ti-HCNFs and Ti-MWCNTs coatings

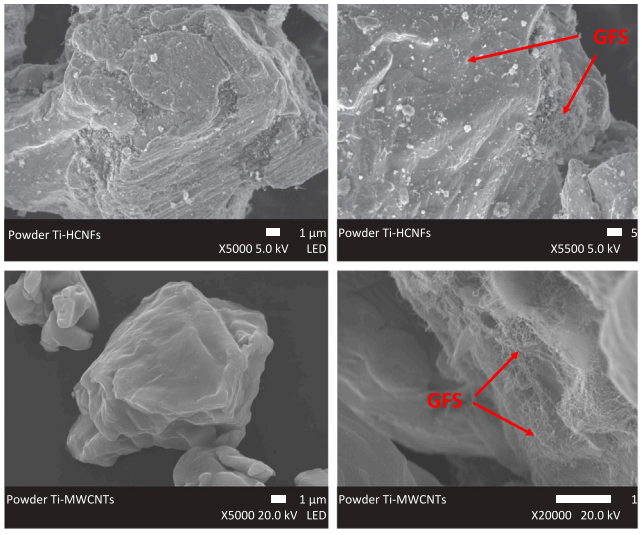

Fig. 5. SEM images Ti-HCNFs and Ti-MWCNT powders.

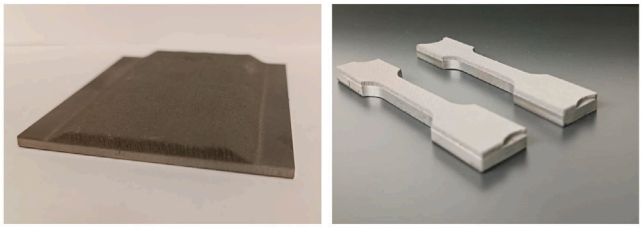

Fig. 6. CGS Ti-GFs coatings.

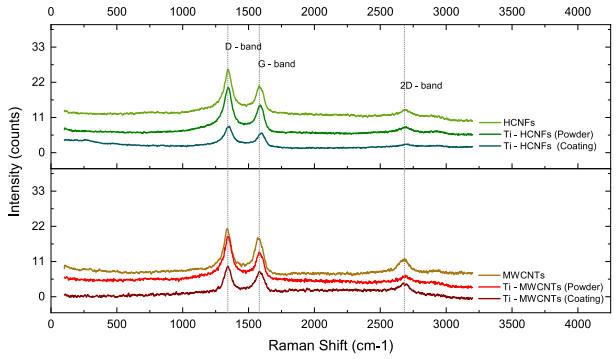

Fig. 7. Raman spectra.

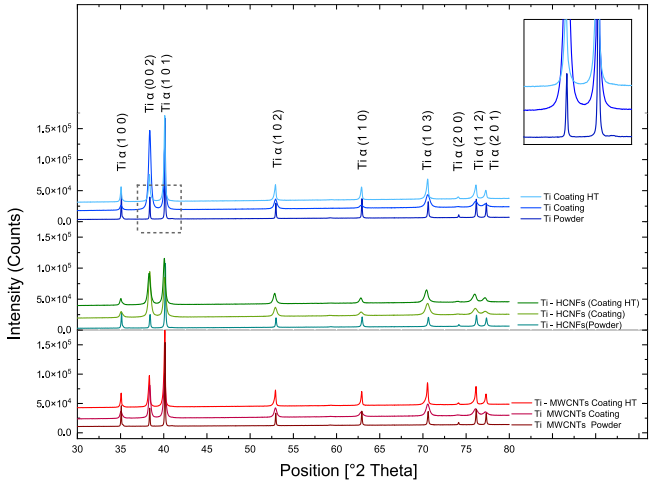

Fig. 8. XRD patterns.

exhibited identical characteristics, featuring the same thickness and surface roughness. Therefore, it can be deduced that incorporating GFs at a content of 0.5 wt% into the Ti matrix does not affect the deposition efficiency or the adhesion of Ti particles in cold spraying.

3.4.1. *Microstructural properties*

The microstructural characterization of CGS Ti and Ti-GFs coatings is shown in Fig. 9. All coatings porosity <1.0%. Adding 0.5 wt% of HCNFs or MWCNTs did not influence the density of the Ti matrix, maintaining a low porosity. This porosity is comparable to the findings reported in the literature [30], where porosities of 1.72 ± 0.10% and 1.81 ± 0.08% were observed for different spraying thicknesses using the same reference Ti powder, albeit with different equipment. The effect of HT on porosity was not noticeable, since the material's density was already considerably high in its As-sprayed state. It is noteworthy that HT did not affect porosity, keeping it below 1.0% across all studied treatment temperatures.

The CGS Ti, and Ti-GFs, coatings exhibited the same microstructural evolution with the applied HT post-treatments. In the As-sprayed condition, deformed particles are more distinctly visible, revealing the interparticular region or the very evident dark-colored particle boundaries, with metallic Ti particles in the clear areas of Fig. 9. With the progression of HT temperature, these particle boundaries are gradually eliminated, resulting in a microstructure of uniformly distributed equiaxed grains at the end of HT at 1000 °C.

The phenomenon that accounts for disappearing interparticular region is the atomic diffusion, which is governed by temperature and time. In As-sprayed condition, particles are severely deformed during the impact onto the substrate, leading to cold working hardening of the Ti matrix, which is more concentrated on the periphery of the particles, where the density of discontinuities and crystalline defects is higher than in the core of each particle [31]. This deformation is the basis for particle adhesion, adiabatic shear instability (ASI), where the formation speed is very high, breaking the particles' oxide layers and generating an intimate connection between the substrate materials and the particles [32].

Energy accumulation due to cold working accelerates the onset of the material's recovery and recrystallization process, reducing its starting temperature or the time for such phenomena [33]. Recovery begins at lower HT temperatures, relieving the material's residual stresses. As the HT temperature increases, recrystallization leads to recovery, nucleating, and growing new α-Ti grains in areas of higher dislocation density, thereby consuming the previous grain boundaries and particles limits in regions of closer adhesion between particles. Interparticular regions remain in the microstructure of Ti and Ti-GFs with HT at 500 °C, seen as dark areas surrounding the particles. However, with HT at 700 °C, the particle boundaries in the coatings become less distinct, and finally, with an HT at 1000 °C, these boundaries do not exist.

The dislocation density, resulting from the material's cold work, and the morphology of the particle boundaries, influence the properties of Ti CGS and Ti-GFs coatings. Table 2 shows the evolution of the coatings' hardness with HT temperature. The recovery and recrystallization phenomena of the Ti matrix had little effect on the hardness of the CGS Ti coating, which remained around 200 $HV_{0.2}$. However, for the CGS Ti-HCNFs and Ti-MWCNTs coatings, the hardness decreased, as shown in Table 2, for an HT temperature of 500 °C, reaching a value very close to that of reference Ti-Bulk, between 170 and 180 $HV_{0.2}$.

But, as the HT temperature was raised to 700 °C and 1000 °C, the hardness increased again, peaking at 229 $HV_{0.2}$. It indicates that a content of 0.5 wt% of GFs induced a microstructural alteration in

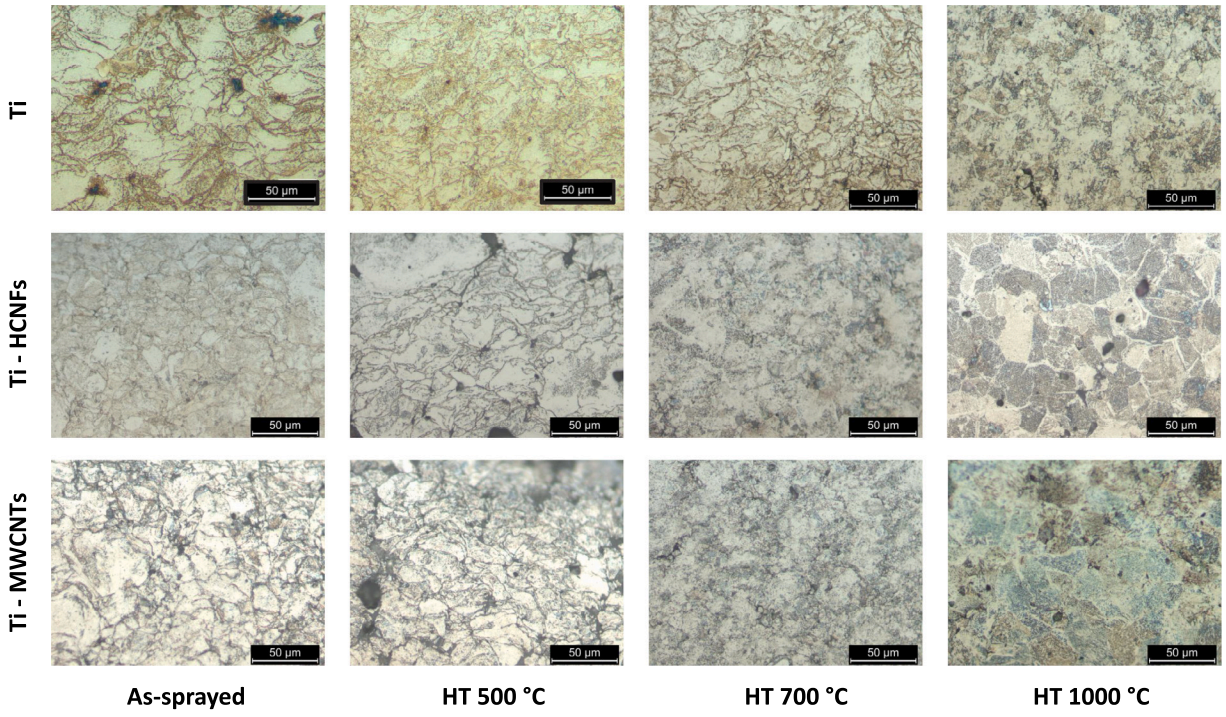

Fig. 9. OM images of etched microstructure of CGS Ti and Ti-GFs coatings.

the Ti matrix, stabilizing a harder microstructure than As-sprayed GFs Ti. The HT at 700 and 1000 °C promote the diffusion of C into the Ti matrix, leading to the formation of TiC, a hard cermet.

However, the low C content around the particles results in the creation of small volumes of finely dispersed TiC in the metallic matrix [34], a Ti MMCs reinforced with TiC, justifying the increase in hardness only for the Ti-GFs and not for the CGS Ti coating.

3.4.2. Fracture cross-section

Fig. 10 provides an additional insight by revealing the fracture cross-section of the CGS Ti-HCNFs coating that was obtained by bending the sample until it fractured and then observed in SEM. The images clearly show that the GR fibers remain firmly adhered to the surface of the Ti particles after the CGS deposition. It demonstrates the ability of the CGS process to maintain effective adhesion of the GR reinforcements, which is essential for load transfer and the improvement of mechanical properties.

Furthermore, Fig. 10 illustrates that the interparticular region within the coating's particles often contain GR clusters, presenting as agglomerated and entangled fibers, which did not achieve complete dispersion during the powder preparation process. These clusters directly contribute to the observed porosity and could potentially affect the coating's properties. Addressing the presence of these agglomerated and entangled fibers is essential for the process optimization, aiming for a more uniform GR dispersion and, consequently, an enhancement in the coating's quality.

The analysis of the Raman spectra in the cross-section of the Ti-HCNFs and Ti-MWCNTs coatings Fig. 7, provides information on how

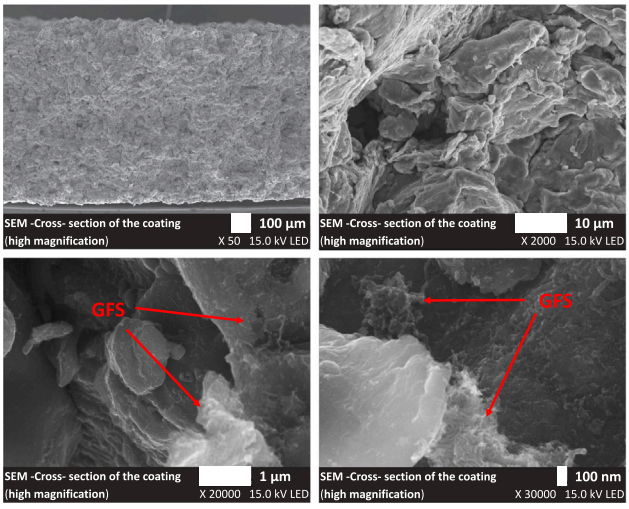

Fig. 10. SEM cross section of CGS Ti-GFs coatings.

the GFs remain embedded within the Ti matrix. The preservation of the original Raman peaks of the GFs after the CGS process indicates that the GR maintains its crystalline structure. In addition, the appearance of new bands or changes in the intensity of existing peaks is not evidenced.

Table 2
Properties of Ti and Ti-GFs coatings.

Material	As-sprayed	Heat Treatment (HT)		
	[$HV_{0.2}$]	500 °C	700 °C	1000 °C
Ti	204 ± 9	202 ± 8	199 ± 2	206 ± 14
Ti-HCNFs	190 ± 13	179 ± 16	196 ± 15	226 ± 16
Ti-MWCNTs	192 ± 16	174 ± 16	196 ± 12	229 ± 22

Table 3
Rietveld refinement results of Ti coating.

Material	RwP	GofF	Crystallite size nm	e, microstrain rms	a Å	c Å
Ti_Powder	4010	3.04	528.0	0.00044	3427	5443
Ti_Coating	2200	2.40	56.0	0.00180	3431	5443
Ti_Coating HT 1000 °C	6300	2.60	118.0	0.00024	3427	5444

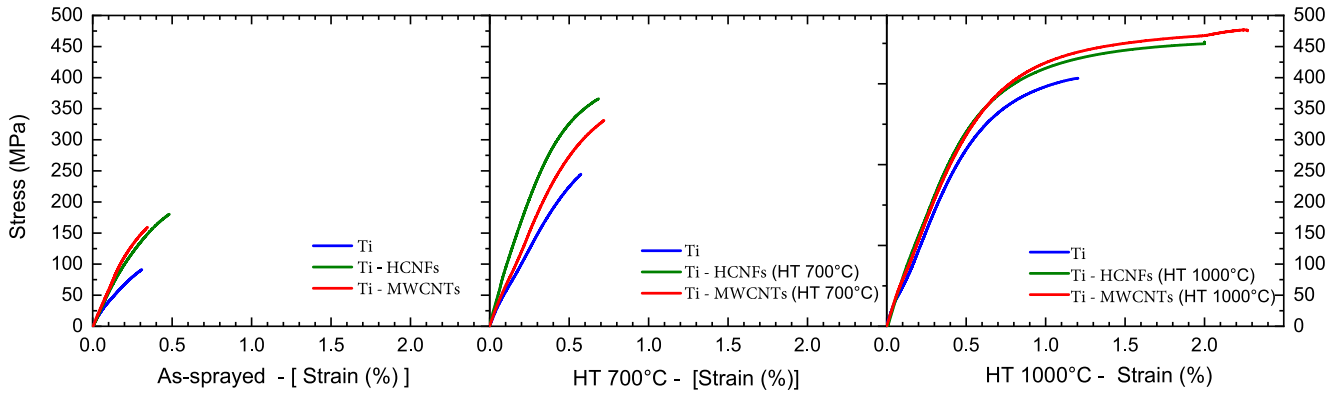

Fig. 11. Tensile test results.

Fig. 8 presents a comparison of the XRD patterns for Ti powder, CGS Ti, Ti-HCNFs, and Ti-MWCNTs coatings is presented. A notable widening in the peaks of the coatings is observed. This phenomenon suggests an alteration in the microstructure of Ti after the CGS deposition. The broadening of the peaks could indicate a modification in the crystalline structure, as a result of residual stresses generation in Ti matrix and the severe plastic deformation experienced by the particles impacting the substrate at high velocity.

The Rietveld refinements results are shown in Table 3. The Rwp and GofF values are below 10%, indicating that the refinement was adequate. It is observed that the sprayed sample has higher FWHM values due to a decrease in crystallite size and an increase in microstrain. This shows a refinement of the microstructure of the powders when they are sprayed. After the heat treatment, the sample shows an increase in crystallite size and a decrease in microstrain, in comparison to As-sprayed sample, which is consistent result of a thermal treatment. In the case of the As-sprayed sample, the increase in microstrain compared to the pure Ti sample suggests the presence of tensile residual stresses, which decrease after heat treatment.

3.4.3. Tensile test results

Fig. 11 shows the results of tensile tests for CGS Ti, Ti-HCNFs, and Ti-MWCNTs coatings. It offers detailed insights into how GFs and HT alter the mechanical characteristics of CGS Ti coating. Initially, the As-sprayed Ti sample shows Ultimate Tensile Strength (σ_u) and Elastic Modulus (E), 91.1 MPa and 29.39 GPa, respectively, with a Deformation (ε) of 0.3%. These values serve as a baseline to evaluate the impacts of GFs and HT on the coating properties.

Notably, As-sprayed Ti-HCNFs exhibit higher σ_u and E, reaching 180.3 MPa and 37.56 GPa, respectively, alongside a higher ε of 0.48%. Conversely, As-sprayed Ti-MWCNTs shows a σ_u of 159.2 MPa and an E of 46.82 GPa, with a ε of 0.34%. These enhancements can be attributed to the effective load transfer from the Ti matrix to the reinforced interfaces. As highlighted by Yi et al. this is attributed to leveraging the strong chemisorption interactions between GFs and Ti, which enhances adhesion and load transfer, thereby improving the composite's strength and stiffness [35,36].

At 700 °C, all samples demonstrate increased tensile strength and E, notably so in reinforced samples. For instance, HT Ti-HCNFs at 700 °C show a Yield Stress (σ_y) of 280 MPa and an E of 73.68 GPa, with a σ_u of 365.96 MPa and a ε of 0.68%, marking a significant enhancement in both strength and ductility. At 1000 °C, these effects amplify, with Ti-HCNFs achieving a σ_y of 314 MPa, an E of 61.57 GPa, and a σ_u of 456 MPa, alongside a remarkable ε of 2.0%. These increases suggest improvements not just in strength and stiffness but also ductility, essential for applications requiring high resilience and energy absorption capacity before failure.

The higher ε observed in samples HT at 1000 °C suggests a beneficial interaction between the Ti matrix and the reinforcement materials under conditions of high temperature, crucial for enabling plastic deformation and enhancing the material toughness. Notably, the Ti-MWCNTs HT at 1000 °C, exhibiting a ε of 2.27%, signifies an optimal synergy between the Ti matrix and MWCNTs facilitating a more uniform stress distribution and promoting efficient deformation mechanisms at elevated temperatures. Despite the absence of TiC phases in XRD analyses and Raman spectra, Fig. 7, the role of charge transfer is pivotal in the observed enhancements in strength, stiffness, and ductility. This is attributed to the strong interactions between GFs forms and Ti, potentially leading to the creation of interfacial structures at nanoscale particle boundaries [37,38].

3.4.4. Wear test by sliding (ball-on-disk)

Fig. 12 presents the CoF evolution during the sliding wear test. The Ti-Bulk with a CoF of 0.724 ± 0.040 establishes a benchmark for comparing the effectiveness of different CGS coatings. The CGS Ti As-sprayed and HT 1000 °C coatings show a significant increase in the CoF, reaching 0.936 ± 0.020 and 0.86 ± 0.041, respectively, which could be related to the deposit microstructure composed by deformed particles and porous retained between the particles during the CGS process.

On the other hand, CGS Ti-HCNFs and Ti-MWCNTs coatings present CoF of 0.739 ± 0.030 and 0.788 ± 0.040, respectively, and the samples HT at 1000 °C Ti-HCNFs and Ti-MWCNTs present CoF 0.758 ± 0.055 and 0.0754 ± 0.045, respectively, showing a reduction in the CoF compared to the CGS Ti coating. These values indicate that GR incorporated into the Ti matrix acts as nano-scale lubricants that facilitate the relative movement between contact surfaces [39,40].

In Fig. 13, the wear tracks from the ball-on-disk test are presented, where it is clear a difference between the Ti-Bulk wear track and the CGS coatings. The first one has a tribolayer formed with oxidized debris adhered to the wear track, darker areas, while all the coatings have many furrows in the direction of the ball sliding. Based on the wear track size and testing parameters it was measured the wear rate for each sample: the Ti-Bulk had a volume loss rate of $6.18 \pm 0.55 \times 10^{-4}$ mm^3/N m, which has served as a benchmark for evaluating CGS coatings.

The Ti As-sprayed and Ti HT coating exhibited a wear rate of $13.05 \pm 33.98 \times 10^{-4}$ and $5.82 \pm 32.08 \times 10^{-4}$ mm^3/N m, respectively. Demonstrating lower wear resistance of Ti As-sprayed compared to the Ti-Bulk, but close results after the HT post-processing. This lower wear resistance in the CGS Ti As-sprayed deposits is attributed to the relatively low cohesion between particles, which causes particle detachment from the deposit under the action of sliding forces during the ball-on-disk test. This phenomenon increases the volume wear rate compared to the reference Ti-Bulk. However, the microstructural changes promoted by the HT at 1000 °C eliminate this low strength inter-particular zone, promoting a crystalline structure similar to the Ti-Bulk, as seen in Fig. 9, with clear consequences on the Ti coating wear performance.

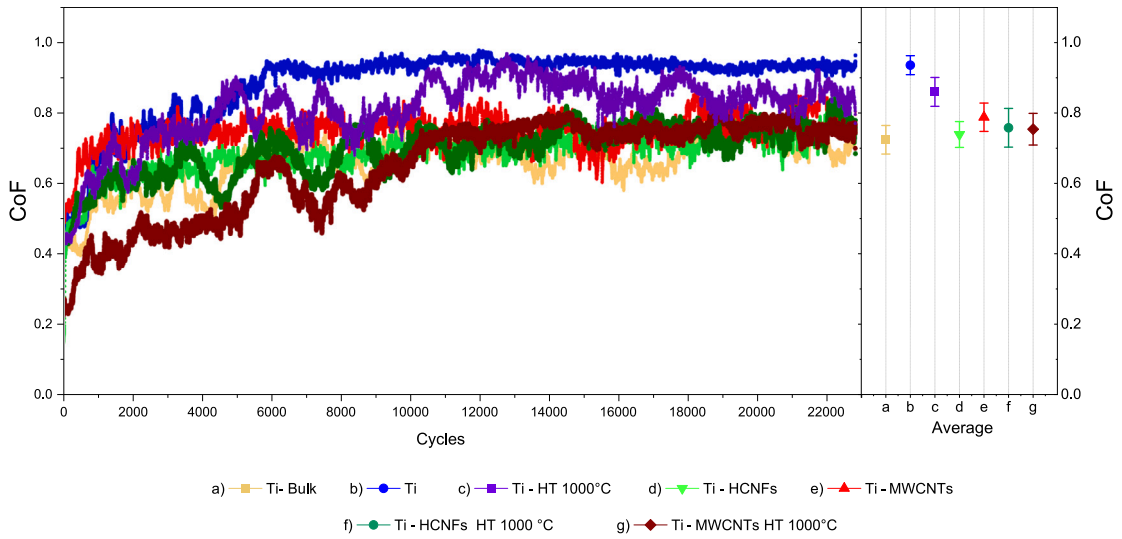

Fig. 12. CoF evolution of CGS Ti, Ti-GFs coatings, and Ti-Bulk.

On the other hand, the Ti-HCNFs and Ti-MWCNTs coatings showed a lower wear rate than CGS Ti, with values of $11.35 \pm 2.45 \times 10^{-4}$ and $10.45 \pm 2.19 \times 10^{-4}$ mm^3/N m, respectively. These results indicate an improvement in wear resistance due to the incorporation of GFs, which act as reinforcements, enhancing the cohesion between the particles in the coating. Additionally, the reinforced coatings HT at 1000 °C showed an even more significant reduction in the wear rate, with values of $3.92 \pm 2.60 \times 10^{-4}$ and $5.05 \pm 1.74 \times 10^{-4}$ mm^3/N m for Ti-HCNFs and Ti-MWCNTs, respectively, which is even lower than the Ti-Bulk benchmark material. This behavior is attributed to the improvement in the coating after the HT, where atomic diffusion results in greater wear resistance by improving the cohesion of the previous deformed particles, and converting them into a crystals structure, as observed previously in microstructural analysis, in Fig. 9.

Although the coatings do not reach the performance levels required for high-wear applications, and considering that Ti is not intrinsically a high performance material for severe wear applications, the CGS deposition technique plays a crucial role. Despite this technique potentially reducing some of the typical properties of Ti, the incorporation of GFs has allowed the preservation of the intrinsic properties of Ti to a large extent, offering a substantial improvement in its tribological behavior for coatings applied through CGS.

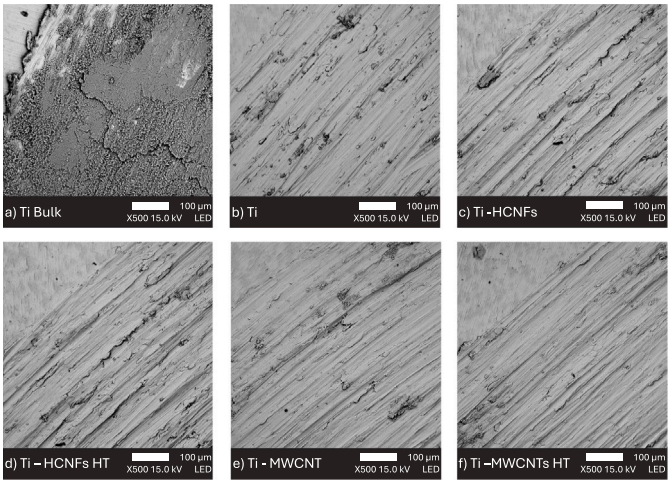

Fig. 13. Ball-on-disk wear track of CGS Ti, Ti-GFs coatings, and Ti-Bulk.

4. Conclusions

With the characterization and evaluation of CGS Ti and Ti-GFs coatings, it can be concluded that:

- The incorporation of HCNFs and MWCNTs 0.5 wt%, into the Ti matrix and subsequent deposition of the coatings using the CGS technique does not change the microstructural properties of CGS Ti coating, such as porosity or hardness, comparing the As-sprayed condition.
- The incorporation of HCNFs and MWCNTs into the Ti matrix improves the CGS coating strength, stiffness, and ductility by improving the particles cohesion.
- HT further enhances strength, stiffness, and ductility, particularly at 1000 °C, indicating improved resilience and toughness suitable for high-performance applications.
- The Ti coatings reinforced with HCNFs and MWCNTs demonstrated a significantly lower CoF compared to CGS applied Ti coatings without reinforcement. This behavior is attributed to the incorporation of carbon nanofibers, which act as nanoscale lubricants, facilitating the relative movement between contact surfaces and thus improving the tribological properties of the coating.
- Although the Ti coatings obtained by CGS showed lower wear resistance compared to Ti Bulk, the addition of HCNFs and MWCNTs improved this property, reducing the wear rate. However, despite these improvements, the wear resistance of the reinforced coatings did not notably surpass that of Ti Bulk. This is mainly because titanium, even when reinforced, is not inherently suitable for applications requiring severe friction resistance. This limitation underscores the need to carefully consider the final applications of these coatings, especially in extreme wear contexts.

Future research should focus on improving the homogeneity of the GFs dispersion without affecting their structure in the Ti matrix, exploring the impact of different concentrations and types of GFs on the properties of the coatings, and developing surface treatments or modifications in the CGS process to maximize the advantages of incorporating GFs. Exploring these areas will not only advance knowledge about Ti-GFs coatings but also expand applications in the industry. Besides that, a study of the impact of GFs reinforcement on corrosion, thermal, and electrical properties of CGS Ti coatings could complement the analysis developed in this work

CRediT authorship contribution statement

Edwin Torres Díaz: Writing – original draft, Methodology, Investigation, Formal analysis, Conceptualization. **Alessio Silvello:** Writing

– review & editing, Supervision, Project administration, Methodology, Funding acquisition, Conceptualization. **Edwin Rua Ramirez:** Resources, Methodology, Investigation. **Rafael Molero Campos:** Validation, Supervision, Resources, Investigation. **Antonio Paton Carrero:** Validation, Supervision, Resources, Investigation. **Rodolpho Fernando Vaz:** Writing – review & editing, Supervision, Methodology, Investigation, Conceptualization. **Irene García Cano:** Writing – review & editing, Supervision, Project administration, Methodology, Funding acquisition, Conceptualization.

Declaration of competing interest

The authors declare that they have no known competing financial interests or personal relationships that could have appeared to influence the work reported in this paper.

Acknowledgments

Funding

This research was funded by Grant PID 2021-128917NA-I00 funded by MICIU/AEI, Spain/10.13039/501100011033 and, as appropriate, by "ERDF A way of making Europe", by "ERDF/EU", by the "European Union" or by the "European Union NextGenerationEU/PRTR, and 2021SGR00712.

Funding Ph.D. Students, Edwin Torres Díaz and Edwin Rúa Ramírez were funded by COLCIENCIAS — Ministry of Science, Technology, and Innovation of Colombia, call for PhD applications 906–2021, and 885–2020.

Data availability

Data will be made available on request.

References

[1] S. Singh, M.R. Hasan, P. Sharma, J. Narang, Graphene nanomaterials: The wondering material from synthesis to applications, Sens. Int. 3 (2022) 100190.
[2] I. Martin-Gullon, J. Vera, J.A. Conesa, J.L. González, C. Merino, Differences between carbon nanofibers produced using fe and Ni catalysts in a floating catalyst reactor, Carbon 44 (8) (2006) 1572–1580.
[3] S. Masroor, Functionalized carbon nanotubes: An introduction, Funct. Carbon Nanotubes Biomed. Appl. (2023) 1–20.
[4] D. Chen, J. Li, K. Sun, J. Fan, Graphene-reinforced metal matrix composites: fabrication, properties, and challenges, Int. J. Adv. Manuf. Technol. 125 (7–8) (2023) 2925–2965.
[5] T.-Y. Liao, A. Biesiekierski, C.C. Berndt, P.C. King, E.P. Ivanova, H. Thissen, P. Kingshott, Multifunctional cold spray coatings for biological and biomedical applications: A review, Prog. Surf. Sci. 97 (2) (2022) 100654.
[6] J. Aslam, C.M. Hussain, R. Aslam, Functionalized Carbon Nanotubes for Biomedical Applications, John Wiley & Sons, 2023.
[7] A. Papyrin, Cold spray technology, Adv. Mater. Process. 159 (9) (2001) 49.
[8] H. Assadi, H. Kreye, F. Gärtner, T. Klassen, Cold spraying–A materials perspective, Acta Mater. 116 (2016) 382–407.
[9] M. Ashokkumar, D. Thirumalaikumarasamy, T. Sonar, S. Deepak, P. Vignesh, M. Anbarasu, An overview of cold spray coating in additive manufacturing, component repairing and other engineering applications, J. Mech. Behav. Mater. 31 (1) (2022) 514–534.
[10] B. Vedhanarayanan, V.K. Praveen, G. Das, A. Ajayaghosh, Hybrid materials of 1D and 2D carbon allotropes and synthetic π-systems, NPG Asia Mater. 10 (4) (2018) 107–126.
[11] S. Yin, Z. Zhang, E.J. Ekoi, J.J. Wang, D.P. Dowling, V. Nicolosi, R. Lupoi, Novel cold spray for fabricating graphene-reinforced metal matrix composites, Mater. Lett. 196 (2017) 172–175.
[12] H. Wu, L. Zhang, C. Liu, Y. Mai, Y. Zhang, X. Jie, Deposition of Zn-G/Al composite coating with excellent cathodic protection on low-carbon steel by low-pressure cold spraying, J. Alloys Compd. 821 (2020) 153483.
[13] Z. Zhao, F. Meng, J. Tang, H. Liu, H. Liu, L. Yang, J. Wang, T. Xiong, A novel method of fabricating an antibacterial aluminum-matrix composite coating doped graphene/silver-nanoparticles, Mater. Lett. 245 (2019) 211–214.
[14] K. Prasad, M. Khalik, N. Hutasoit, R.R. Rashid, R. Rashid, A. Duguid, S. Palanisamy, Printability of low-cost pre-heat-treated ball milled Al7075 powders using compressed air assisted cold spray additive manufacturing, Addit. Manuf. Lett. 3 (2022) 100046.
[15] L. Zhang, G. Hou, W. Zhai, Q. Ai, J. Feng, L. Zhang, P. Si, L. Ci, Aluminum/graphene composites with enhanced heat-dissipation properties by in-situ reduction of graphene oxide on aluminum particles, J. Alloys Compd. 748 (2018) 854–860.
[16] K. Prasad, R.A. Rahman Rashid, N. Hutasoit, S. Palanisamy, N. Hameed, Fabrication of metal/graphene composites via cold spray process: State-of-the-art and the way forward, C 8 (4) (2022) 65.
[17] W. Zhang, S. Zhou, W. Ren, Y. Yang, L. Shi, Q. Zhou, M. Liu, Uniformly dispersing GNPs for fabricating graphene-reinforced pure Ti matrix composites with enhanced strength and ductility, J. Alloys Compd. 888 (2021) 161527.
[18] S. Yin, C. Chen, X. Suo, R. Lupoi, Cold-sprayed metal coatings with nanostructure, Adv. Mater. Sci. Eng. 2018 (2018).
[19] ASTM International, Standard specification for titanium and titanium alloy bars and billets, 2019, ASTM B348.
[20] ASTM International, Standard practice for verification and classification of extensometer systems, 2023, ASTM E83.
[21] ASTM International, Standard test methods for flow rate of metal powders using the hall flowmeter funnel, 2020, ASTM B213-20.
[22] ASTM International, Standard guide for metallographic preparation of thermal sprayed coatings, 2021, ASTM E1920.
[23] ASTM International, Standard test methods for determining area percentage porosity in thermal sprayed coatings, 2021, ASTM E2109.
[24] ASTM International, Standard test method for microindentation hardness of materials, 2017, ASTM E384-99.
[25] ASTM International, Standard test methods for tension testing of metallic materials, 2022, ASTM E8.
[26] International Organization for Standardization, Metallic materials - calibration of extensometer systems used in uniaxial testing, 2023, ISO 9513.
[27] ASTM International, Standard test method for wear testing with a pin-on-disk apparatus, 2015, ASTM G99.
[28] W. Wong, P. Vo, E. Irissou, A. Ryabinin, J.-G. Legoux, S. Yue, Effect of particle morphology and size distribution on cold-sprayed pure titanium coatings, J. Therm. Spray Technol. 22 (2013) 1140–1153.
[29] T. Schmidt, F. Gärtner, H. Assadi, H. Kreye, Development of a generalized parameter window for cold spray deposition, Acta Mater. 54 (3) (2006) 729–742.
[30] R.F. Váz, A. Silvello, P.D. Cavalière, S. Dosta, I.G. Cano, L. Capodieci, A. Rizzo, D. Valerini, Fretting wear and scratch resistance of cold-sprayed pure Cu and Ti, Metallogr. Microstruct. Anal. 10 (2021) 496–513.
[31] T. Liu, J.D. Leazer, L.N. Brewer, Particle deformation and microstructure evolution during cold spray of individual Al-Cu alloy powder particles, Acta Mater. 168 (2019) 13–23.
[32] H. Assadi, F. Gärtner, T. Klassen, H. Kreye, Comment on 'Adiabatic shear instability is not necessary for adhesion in cold spray', Scr. Mater. 162 (2019) 512–514.
[33] H. Xue, H. Yuan, K. Guo, Z. Zhang, M. Zhang, Microstructure evolution and recrystallization temperature change of cold-rolled Fe–19Mn–0.6 C twinning-induced plasticity steel during annealing, Metals 11 (8) (2021) 1181.
[34] A.F. Fonseca, T. Liang, D. Zhang, K. Choudhary, S.R. Phillpot, S.B. Sinnott, Titanium-carbide formation at defective curved graphene-titanium interfaces, MRS Adv. 3 (8–9) (2018) 457–462.
[35] C. Yi, S. Bagchi, C.M. Dmuchowski, F. Gou, X. Chen, C. Park, H.B. Chew, C. Ke, Direct nanomechanical characterization of carbon nanotubes-titanium interfaces, Carbon 132 (2018) 548–555.
[36] K. Liu, J. Li, J. Wan, Q. Yan, K. Kondoh, J. Shen, S. Li, B. Chen, Sintering-free fabrication of high-strength titanium matrix composites reinforced with carbon nanotubes, Carbon 197 (2022) 412–424.
[37] Z. Wei, Y. Han, S. Li, N. Zong, J. Le, S. Zhang, J. Chen, S. Zhong, G. Huang, W. Lu, Interfacial modification strategy to break through the strength and ductility trade-off in multi-walled carbon nanotubes reinforced titanium matrix composites, Mater. Sci. Eng. A (2023) 145284.
[38] L. Wei, X. Liu, Y. Gao, X. Lv, N. Hu, M. Chen, Synergistic strengthening effect of titanium matrix composites reinforced by graphene oxide and carbon nanotubes, Mater. Des. 197 (2021) 109261.
[39] W. Zhai, N. Srikanth, L.B. Kong, K. Zhou, Carbon nanomaterials in tribology, Carbon 119 (2017) 150–171.
[40] K. Yang, F. Zhang, R. Wang, Y. Xiong, J. Tang, H. Chen, M. Duan, Z. Li, H. Zhang, B. Xiong, Review of two-dimensional nanomaterials in tribology: Recent developments, challenges and prospects, Adv. Colloid Interface Sci. (2023) 103004.